

Warm molecular hydrogen in outflows from Ultraluminous Infrared Galaxies

Matthew J. Hill^{1*}, Nadia L. Zakamska^{1†}

¹*Department of Physics & Astronomy, Johns Hopkins University, 3400 N. Charles St., Baltimore, MD 21218, USA*

21 January 2019

ABSTRACT

Ultraluminous infrared galaxies (ULIRGs) show on average three times more emission in the rotational transitions of molecular hydrogen than expected based on their star formation rates. Using *Spitzer* archival data we investigate the origin of excess warm H_2 emission in 115 ULIRGs of the IRAS 1 Jy sample. We find a strong correlation between H_2 and [Fe II] line luminosities, suggesting that excess H_2 is produced in shocks propagating within neutral or partially ionized medium. This view is supported by the correlations between H_2 and optical line ratios diagnostic of such shocks. The galaxies powered by star formation and those powered by active nuclei follow the same relationship between H_2 and [Fe II], with emission line width being the major difference between these classes (~ 500 and ~ 1000 km/sec, respectively). We conclude that excess H_2 emission is produced as the supernovae and active nuclei drive outflows into the neutral interstellar medium of the ULIRGs. A weak positive correlation between H_2 and the length of the tidal tails indicates that these outflows are more likely to be encountered in more advanced mergers, but there is no evidence for excess H_2 produced as a result of the collision shocks during the final coalescence.

Key words: galaxies: active – galaxies: interactions – galaxies: ISM – galaxies: starburst

1 INTRODUCTION

Although the amount of molecular hydrogen H_2 in gas-rich galaxies can reach $> 10^{10} M_\odot$ (Solomon et al. 1997), the rotational transitions of H_2 in the mid-infrared and the ro-vibrational transitions in the near-infrared are relatively weak. One reason is that the rotational transitions are quantum-mechanically forbidden; another is that most molecular gas is at a temperature of just a few tens of K (Draine 2011), much smaller than the temperature required to populate even the lowest excited levels of H_2 (e.g., $E_{J=2} = k_B \times 518$ K). Thus the H_2 we observe in the mid-infrared is “warm” molecular hydrogen which represents only a small fraction of the total H_2 present in the galaxy (Higdon et al. 2006).

Emission of warm H_2 in star-forming galaxies is a minor by-product of star formation, contributing only a small fraction ($< \text{a few} \times 10^{-4}$) of the total infrared luminosity of the galaxy (Roussel et al. 2007). The dominant source of excitation of the observed emission of molecular hydrogen H_2 is likely in photo-dissociation regions around young stars (Shull & Beckwith 1982; Hollenbach & Tielens 1997). The strong correlation between the mid-infrared H_2 emission and the star formation rate over several orders of magnitude in galaxy luminosity (Roussel et al. 2007) sup-

ports this view. In this case, the dominant process of H_2 excitation is due to ultra-violet photons of newly formed massive stars, which either pump H_2 molecules straight into excited electronic states or heat the surrounding dust which then heats the gas.

In an unexpected challenge to this picture, multiple *Spitzer* observations uncovered extragalactic objects with unusually high rotational H_2 luminosities in which little or no star formation was seen (Appleton et al. 2006; Egami et al. 2006; Ogle et al. 2007; Johnstone et al. 2007). Within this sample, there may be several distinct physical processes responsible for H_2 excitation. In the first class are objects associated with large-scale shocks, either due to relativistic jets (Ogle et al. 2010) or galaxy collisions (Appleton et al. 2006; Ogle et al. 2007; Guillard et al. 2009) or infall of intra-cluster gas onto the central cluster galaxy (Egami et al. 2006). In the second class are intra-cluster filaments where H_2 is seemingly excited by the deposition of cosmic rays into molecular gas (Johnstone et al. 2007; Ferland et al. 2008). Furthermore, the molecular gas in central cluster galaxies may be heated by electrons from the hot cluster atmosphere (Donahue et al. 2011).

The phenomenon of excess emission from warm molecular hydrogen ($T \sim \text{a few hundred K}$) has now been observed in a wide range of objects and environments, from spiral galaxies (Beirão et al. 2009) to active nuclei (Dasyra & Combes 2011) to Galactic translucent clouds (Ingalls et al. 2011). Not only does the molecular gas at these relatively warm temperatures constitute an

* E-mail: mhill@pha.jhu.edu

† E-mail: zakamska@pha.jhu.edu

unusual phase of the interstellar medium, but this gas is typically found out of the dynamic equilibrium with the rest of the galaxy and is often a signature of feedback, whether due to star formation (Roussel et al. 2007; Veilleux, Rupke & Swaters 2009) or accretion onto a supermassive black hole (Nesvadba et al. 2010; Ogle et al. 2010; Dasyra & Combes 2011).

The amount of H_2 emission seen from ultraluminous infrared galaxies (ULIRGs) is also in excess of that expected from star formation alone (Zakamska 2010), by about a factor of three or more. In this paper we investigate the nature of the H_2 emission in these objects. Our sample and data are described in Sec. 2. In Sec. 3, we discuss the relationship between the warm molecular gas emission and the global morphological properties of the galaxies. In Sec. 4 we discuss the relationships between different phases of the gas: molecular, neutral and warm ionized. We present our conclusions in Sec. 5. We use an $h = 0.7$, $\Omega_m = 0.3$, $\Omega_\Lambda = 0.7$ cosmology throughout this paper. Wavelengths of emission lines are given in air, except in Section 2.4 where we discuss fits to Sloan Digital Sky Survey spectra which use vacuum wavelengths. In these cases, the vacuum wavelengths are marked with ‘v’.

To evaluate the significance of weak correlations, we use the Spearman rank test, and to evaluate the similarity of distributions we use the Kolmogorov-Smirnov (KS) test. For both tests we report the probability of the null hypothesis as p_S or p_{KS} – in the first case, the probability that the two sets of data are uncorrelated and in the second case, that the two sets are drawn from the same distribution. Small values of p_S indicate the presence of a statistically significant correlation and small values of p_{KS} indicate a statistically significant difference between two distributions.

2 SAMPLE, DATA AND MEASUREMENTS

2.1 Sample selection

We start with the Infrared Astronomical Satellite (IRAS) 1 Jy sample of 118 ULIRGs (Kim & Sanders 1998). These sources are selected from the IRAS Faint Source Catalog to have flux $F_\nu(60\mu m) > 1$ Jy and are constrained to be at high Galactic latitudes $|b| > 30^\circ$ and declinations $\delta > -40^\circ$. The objects cover a redshift range $z = 0.02 - 0.27$ and the infrared luminosity range $\log(L_{IR}/L_\odot) = 12.00 - 12.90$. Because the spatial resolution of IRAS is $\gtrsim 1'$, a single IRAS source can be composed of two or more individual galaxies which are not resolved individually in the IRAS catalog.

We search *Spitzer* Legacy Archive for low-resolution Infrared Spectrograph (IRS, Houck et al. 2004) data within $60''$ of the nominal position of each target. We use the enhanced spectroscopic data products supplied by the *Spitzer* Science Center (SSC), in which the spectrum has been extracted, background-subtracted and flux-calibrated using the standard spectroscopic pipeline. In many cases, multiple separate visits to the same target are available in the archive. We combine all such spectra into one using error-weighted averages. The close interacting pairs present a more difficult issue. In some such cases only one component of the pair has a spectrum in the archive, and sometimes both do. If the components are closer than $4''$ on the sky – comparable to or smaller than the IRS slit size – we consider them to be unresolved by the IRS and combine such spectra into one. If they are further apart, we consider them as separate sources. We remove the 5 objects where only the short-wavelength orders are available.

Our final sample is defined by the 115 distinct *Spitzer* spectra

Table 1. ULIRGs from IRAS 1 Jy Sample that have *Spitzer* spectra

IRAS Name (1)	Redshift (2)	R.A. (3)	Decl. (4)	Mult. Factor (5)
IRAS 00091-0738	0.118	2.930210	-7.368560	0.878
IRAS 00188-0856	0.128	5.360330	-8.657530	1.000
...
IRAS 01003-2238	0.118	15.708080	-22.365917	0.956
IRAS 01166-0844:NW	0.118	19.781460	-8.485940	0.220
IRAS 01166-0844:SE	0.118	19.782673	-8.486669	1.000
...

Notes. – (1) IRAS Name, supplemented by component designation if necessary using images from Kim, Veilleux & Sanders (2002) (e.g., IRAS 01166-0844:NW for the North-Western component of IRAS 01166-0844). (2) Redshift from Kim & Sanders (1998). (3) Right Ascension of *Spitzer* pointing at J2000.00 epoch in degrees. (4) Declination of *Spitzer* pointing at J2000.00 epoch in degrees. (5) Multiplicative factor used to correct for aperture size difference in SL and LL slits.

(A full version of this table is available in the online journal.)

(some of which are individual components within a single IRAS source) with both short-low (SL) observations with wavelength coverage $5.2 - 14.5\mu m$ and slit dimensions $4.7'' \times 11.3''$ and long-low (LL) observations with wavelength coverage $14.0 - 38.0\mu m$ and slit dimensions $11.1'' \times 22.3''$. We present the sample in Table 1 using the IRS pointing information for precise identification of the sources (keywords RA_RQST and DEC_RQST in the SSC spectroscopic reductions). There is often a discrepancy between the flux normalization in the LL orders and the SL orders, in that LL fluxes are higher. This is most likely due to the difference in apertures: LL aperture is larger and lets in more flux for extended objects. In such cases we apply a multiplicative factor (≤ 1) to the LL spectrum to bring it in agreement with the SL one at $14\mu m$. The factors are listed in Table 1. The final combined and renormalized spectra are available as ASCII files in the online edition of the journal.

2.2 Analysis of *Spitzer* spectra

The spectrum of rotational transitions of H_2 is composed of transitions from rotational energy levels with quantum numbers $J + 2$ to those with quantum numbers J ; the corresponding emission features are denoted S(J). We measure the fluxes of S(1) and S(3) molecular hydrogen emission lines by fitting a Gaussian profile with a quadratic continuum to a cropped section of the spectrum; the other rotational H_2 lines are much weaker and are not detected in most spectra. To check the validity of our flux measurements we compare with measurements of a sample of ULIRGs by Higdon et al. (2006). There are 26 objects shared between the samples. In 20 of them, the measurements of S(1) and S(3) fluxes by Higdon et al. (2006) and us agree within 1σ , whereas in the remaining 6 they agree within 3σ . We assume rest-frame centroids of the lines to be at $17.0346\mu m$ and $9.6649\mu m$, and we use optical redshifts from Kim & Sanders (1998) to find the observed wavelengths of the features. The extraction regions are set to $16.6-17.3\mu m$, $9.1-10.2\mu m$ and $5.23-5.46\mu m$ to avoid other strong emission features. We allow a slop in line centroid of $0.05\mu m$ to account for a possible uncertainty in the redshift and in the IRS wavelength calibration. While the widths of the lines are not fixed in the fit, we find that they agree well with those expected due to the instrumental resolution (Smith et al. 2007) which varies between $R = \lambda/\Delta\lambda = 64 - 128$ as a function of the observed wavelength. Example fits are shown in Figure 1.

Table 2. Mid-Infrared Properties: H₂ and [Fe II] emission

IRAS Name (1)	$L[S(1)]$ (2)	$\sigma[S(1)]$ (3)	$L[S(3)]$ (4)	$\sigma[S(3)]$ (5)	T_{exc} (6)	$\sigma[T_{\text{exc}}]$ (7)	$L[\text{Fe II}]$ (8)	$\sigma[\text{Fe II}]$ (9)	EW PAH[6.2 μm] (10)	$\sigma(\text{EW})$ PAH[6.2 μm] (11)
IRAS 00091-0738	37.70	3.682	10.14	3.140	324	23	11.46	4.277	0.202	0.02460
IRAS 00188-0856	31.41	6.645	20.61	3.601	402	30	8.287	5.429	0.246	0.00986
IRAS 00397-1312	98.40	15.37	411	18	106.9	74.66	0.053	0.00134
IRAS 00456-2904	28.36	3.001	19.66	1.709	408	15	16.84	3.287	1.399	0.8211
IRAS 00482-2720	67.27	9.092	11.96	3.650	297	20	1.057	0.2809

Notes. – (1) Object IRAS Name. (2,3) Luminosity of S(1) emission line in $10^{40} \text{ erg s}^{-1}$ and its uncertainty. (4,5) Luminosity of S(3) emission line in $10^{40} \text{ erg s}^{-1}$ and its uncertainty. (6,7) Excitation temperature derived from S(3)-S(1) transition in degrees K and its uncertainty. (8,9) Luminosity of [Fe II] $\lambda 5.34\mu\text{m}$ in $10^{40} \text{ erg s}^{-1}$ and its uncertainty. (10,11) Equivalent width of the PAH[6.2 μm] in microns and its uncertainty.

(A full version of this table is available in the online journal.)

The population of each energy level can be calculated from the measured flux of the transition:

$$N_{J+2} = \frac{4\pi D_L^2 F_J}{A_{J+2 \rightarrow J}(E_{J+2} - E_J)}, \quad (1)$$

where F_J is the line flux, D_L is the luminosity distance, and A are the Einstein coefficients (Turner, Kirby-Docken & Dalgarno 1977). Here $E_{J+2} - E_J$ is the energy of the transition (equal to the energy of each emitted photon), with energy levels given by Huber & Herzberg (1979) and Landau & Lifshitz (1991) as:

$$E_J = 85.35K \cdot k_B J(J+1) - 0.068K \cdot k_B J^2(J+1)^2, \quad (2)$$

where k_B is the Boltzmann constant. The excitation temperature is related to level populations via

$$\frac{N_J}{g_J} \propto \exp\left(-\frac{E_J}{k_B T_{\text{exc}}}\right), \quad (3)$$

where g_J is the degeneracy of the levels, with $g_J = 3(2J+1)$ for odd J and $g_J = 2J+1$ for even J . Thus, the excitation temperature can be calculated given any two or more line fluxes.

Normally a wide range of excitation temperatures is present, resulting in a non-linear relationship between $\ln(N_J/g_J)$ and E_J (Armus et al. 2006). Typical two-temperature fits to this relationship in ULIRGs (Higdon et al. 2006) reveal a large mass ($\sim 10^9 M_\odot$) of colder ($T \lesssim 300\text{K}$) gas producing emission in low- J transitions and a much lower mass ($\sim 10^6 M_\odot$) of warmer ($T \gtrsim 1000\text{K}$) gas that dominates high- J fluxes. But it is likely that in every object there is a distribution of gas masses as a function of temperature (Zakamska 2010). In what follows we utilize only the excitation temperature T_{exc} between levels $J = 3$ and $J = 5$ measured using the S(1) and the S(3) transitions, with uncertainty in T_{exc} derived through propagation of uncertainties of the S(1) and S(3) line fluxes following equation (3). In a subsample of ULIRGs presented here, Zakamska (2010) derives excitation temperatures using S(1), S(2) and S(3) lines and finds a median temperature of 330 K, lower than the median temperature of 406 K calculated using just the S(1) and S(3) lines. This is not surprising because including the S(2) line flux has the effect of giving more statistical weight to the lower- J transitions whose flux is dominated by emission from lower temperature gas. For some of the objects in our sample it would be possible to construct more detailed excitation diagrams and multi-temperature fits, but in most cases because of the low signal-to-noise of the data we can measure only these two strongest H₂ lines, and thus we restrict ourselves to this simple measure. Physically, the T_{exc} that we measure may be interpreted in terms of the slope of the mass-temperature distribution, or in terms of the ratio of mass of the warmer component to that of the cooler component.

We use the emission of polycyclic aromatic hydrocarbons (PAH; Allamandola, Tielens & Barker 1989) as a measure of star formation (Roussel et al. 2001; Dale & Helou 2002). PAH fluxes are calculated by cutting out a $\lesssim 3\mu\text{m}$ -wide part of the spectrum, excluding other features in that wavelength range, and then modeling this cut-out using a polynomial continuum and Drude (damped harmonic oscillator) profiles with profile shapes and widths taken from Smith et al. (2007). For PAH complexes, such as those at 11.3 μm and at 7.7 μm , the relative amplitudes of the components within the complex are fixed to their ratios in the template spectrum of normal star-forming galaxies (Smith et al. 2007). For example, within the 11.3 μm complex the amplitude ratio of the 11.23 μm and 11.33 μm components is fixed to 1.25:1. Depending on the model for the local continuum, from a constant to a cubic polynomial, the number of fit parameters varies from two to five, with the amplitude being the only parameter that describes the intensity of the PAH feature (since the functional shape of the feature remains fixed). Example fit is shown in Figure 1. The quality of fits to PAH features is typically very good, and most are detected in almost all objects with high confidence.

The powering source of ULIRGs (star formation and/or accretion onto a supermassive black hole) is often hidden behind large amounts of dust and gas, which may be optically thick even at mid-infrared wavelengths. We parametrize the dust obscuration using the apparent strength of silicate absorption defined as $\tau[9.7\mu\text{m}] = -\ln(f_{\text{obs}}[9.7\mu\text{m}]/f_{\text{cont}}[9.7\mu\text{m}])$, where f_{obs} is the observed flux density and f_{cont} is the guess for the local continuum. To estimate f_{cont} , we average emission in the wavelength ranges 5.3 – 5.6 μm and 13.85 – 14.15 μm and then interpolate between these points using a power-law. In the calculation of f_{obs} , the S(3) line is excluded and the continuum within the absorption trough is fitted with a second order polynomial. Negative values of $\tau[9.7\mu\text{m}]$ indicate silicate emission, while positive values indicate absorption, with $\tau[9.7\mu\text{m}] \simeq 3.5$ for the most absorbed sources. This method is almost identical to that used by Spoon et al. (2007); the minor difference at high optical depths is that we do not use a continuum point at 7.7 μm even in the cases of weak PAH emission. The apparent strength of Si absorption defined this way is closely related to, but not identical to the optical depth of Si dust absorption; depending on the continuum opacity of the dust at these wavelengths, the actual optical depth is $\simeq (1.2 - 1.5) \times$ the apparent strength of the Si feature.

Many other emission features are present in *Spitzer* spectra. The one of particular interest to us is the [Fe II] $\lambda 5.34\mu\text{m}$ emission line which we measure using the same method (single Gaussian fit) as the H₂ emission. Measurements made from *Spitzer* spectra are given in Tables 2 and 3.

Table 3. Mid-Infrared Properties: Si absorption and PAH emission

IRAS Name (1)	$\tau[9.7\mu\text{m}]$ (2)	$L[6.2\mu\text{m}]$ (3)	$\sigma[6.2\mu\text{m}]$ (4)	$L[7.7\mu\text{m}]$ (5)	$\sigma[7.7\mu\text{m}]$ (6)	$L[8.5\mu\text{m}]$ (7)	$\sigma[8.5\mu\text{m}]$ (8)	$L[11.3\mu\text{m}]$ (9)	$\sigma[11.3\mu\text{m}]$ (10)
IRAS 00091-0738	2.70	4.92	0.69	39.28	5.59	0.00	1.13	4.93	0.54
IRAS 00188-0856	2.53	10.34	0.82	60.74	10.25	16.75	1.15	8.62	0.56
IRAS 00397-1312	2.51	76.35	6.86	252.40	30.09	0.00	10.03	29.41	1.56
IRAS 00456-2904	0.82	18.42	1.13	68.32	2.19	22.51	1.17	12.52	0.58
IRAS 00482-2720	2.13	5.00	0.55	16.30	1.83	4.53	1.10	2.58	0.54

Notes. – (1) Object IRAS Name. (2) Strength of the silicate feature at $9.7\mu\text{m}$. (3,4) Luminosity of PAH[6.2 μm] emission feature in $10^{42}\text{ erg s}^{-1}$ and its uncertainty. (5,6) Luminosity of PAH[7.7 μm] emission feature in $10^{42}\text{ erg s}^{-1}$ and its uncertainty. (7,8) Luminosity of PAH[8.5 μm] emission feature in $10^{42}\text{ erg s}^{-1}$ and its uncertainty. (9,10) Luminosity of PAH[11.3 μm] emission feature in $10^{42}\text{ erg s}^{-1}$ and its uncertainty. (A full version of this table is available in the online journal.)

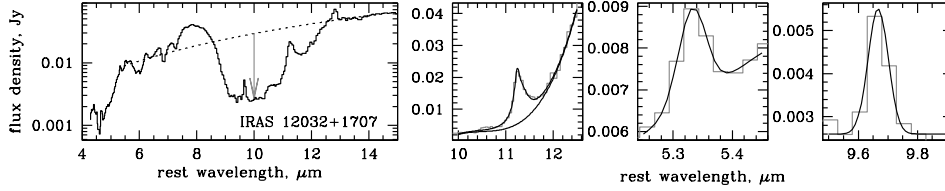


Figure 1. Left: Example IRS spectrum of one of the objects in our sample. The dashed line shows the interpolated power-law continuum and the arrow shows the measurement of the strength of the silicate feature, $\tau[9.7\mu\text{m}]$. Right: fits to the PAH[11.3 μm] feature, to the [Fe II] $\lambda 5.34\mu\text{m}$ line and to the S(3) line of molecular hydrogen.

2.3 Optical and near-infrared morphologies

The vast majority of ULIRGs show signs of on-going or recent merger activity (Sanders & Mirabel 1996) and are likely fueled by star formation in major gas-rich mergers (Dasysra et al. 2006). We use optical and near-infrared data to determine the stage of the merger and to provide quantitative measures along the merger sequence. Because of projection effects, such measures are only approximate.

A number of useful measurements of the IRAS 1 Jy sample are available in the literature. High-quality seeing-limited optical (R -band) and near-infrared (K' -band) images of IRAS 1 Jy sample are presented by Kim, Veilleux & Sanders (2002), and measurements of nuclear separation and tidal tail length and merger stage classification are presented by Veilleux, Kim & Sanders (2002). Nuclear separations can be measured down to the seeing limit of approximately $1'' \sim 3\text{ kpc}$. The lengths of tidal tails are recorded by measuring along each tail down to a constant surface brightness of 24 mag/arcsec^2 in R -band images.

Veilleux, Kim & Sanders (2002) use these measurements as well as their imaging observations (Kim, Veilleux & Sanders 2002) to classify the merger stage of each object in the IRAS 1 Jy sample. These authors find that the combination of morphological features and the high infrared luminosities of ULIRGs indicate that the vast majority of the merging galaxies in these systems have already made the first close approach. This is likely a selection effect: only systems with the highest star formation rate have high enough luminosities to be classified as ULIRGs, and only the systems past their first approach have had enough of a potential perturbation to funnel enough gas into the centres of participating galaxies (Barnes & Hernquist 1991, 1996; Mihos & Hernquist 1994, 1996). Thus, Veilleux, Kim & Sanders (2002) place almost all ULIRGs into the III, IV, and V merger classes of their classification scheme,

Table 4. Morphological and spectral classification

IRAS Name (1)	NS ^a (2)	TL ^a (3)	MS ^a (4)	ST ^b (5)
IRAS 00091-0738	2.1	12.0	pre-merger	cp
IRAS 00188-0856	0.0	0.0	old merger	S2
IRAS 00397-1312	0.0	0.0	old merger	cp
IRAS 00456-2904	20.7	9.0	pre-merger	cp
IRAS 00482-2720	6.7	15.0	pre-merger	cp

Notes. – (1) Object IRAS Name. (2) Projected nuclear separation measured in kpc. (3) Length of tidal tails measured in kpc. (4) Merger stage. (5) Spectral type.

^a Veilleux, Kim & Sanders (2002)

^b Yuan, Kewley & Sanders (2010)

(A full version of this table is available in the online journal.)

skipping I and II (which correspond to before and during the closest approach). Following Veilleux, Kim & Sanders (2002), we refer to classes III, IV and V as Pre-merger, Merger and Old Mergers respectively.

Pre-merger systems are characterized by having two distinguishable nuclei as well as strong tidal features (which tend to develop after the first closest approach, Toomre & Toomre 1972). Merger systems have a single detectable nucleus as well as strong tidal features, as well as an extended nuclear region. Old Mergers differ from Merger in that show no clear signs of tidal feature, but still have a disturbed central morphology indicative of a past merger event. In our sample of 115 systems, 49 have two distinguishable nuclei (Pre-Mergers), 48 are in the Merger stage and 12 are Old Mergers (Table 4). There are also 5 galaxies in triple systems and 1 isolated non-interacting galaxy.

2.4 Optical and near-infrared spectroscopic data

Optical and near-infrared spectra of ULIRGs show prominent emission lines produced in ionized gas. We use optical classifications by Yuan, Kewley & Sanders (2010) to determine the dominant source of gas ionization. The first step is identification of objects with broad emission lines (FWHM \sim a few thousand km sec^{-1} for $\text{H}\beta$ and other permitted transitions), which are classified as optically unobscured active galactic nuclei (AGNs). For objects that have only narrow emission lines, standard diagnostic diagrams are used to determine the source of the ionization. Among our sample, 9 objects are classified as type 1 (broad-line) AGNs, 28 objects are type 2s (narrow-line, but with line ratios characteristic of photo-ionization by an obscured AGN), 13 objects are purely star-forming, 53 are star formation / AGN composites and 3 are low-ionization narrow emission-line region galaxies; 9 objects are left unclassified (Table 4).

Furthermore, we use optical line flux measurements by Veilleux, Kim & Sanders (1999) which are obtained by fitting a Gaussian profile with a first-order polynomial continuum to host-subtracted spectra. We use these to construct diagnostic line ratios $[\text{O I}]\lambda 6300\text{\AA}/\text{H}\alpha$, $[\text{N II}]\lambda 6583\text{\AA}/\text{H}\alpha$ and $[\text{S II}]\lambda\lambda 6716, 6731\text{\AA}/\text{H}\alpha$ and to calculate the Balmer decrement $\text{H}\alpha/\text{H}\beta$. These measurements are available for >90 per cent of the objects in our sample (Table 5).

Additionally, we use $[\text{Fe II}]\lambda 1.644\mu\text{m}$ and $\text{Pa}\alpha$ fluxes from the near-infrared spectroscopic survey of ULIRGs by Veilleux, Sanders & Kim (1997). Because of the weakness of the $[\text{Fe II}]\lambda 1.644\mu\text{m}$ emission line, the $[\text{Fe II}]\lambda 1.644\mu\text{m}/\text{Pa}\alpha$ measurements are available only for 10 objects.

Finally, we search the spectroscopic database¹ of the Sloan Digital Sky Survey (York et al. 2000) within $5''$ of the IRS positions of all our objects. Because some objects are found in close pairs, we examine all possible matches visually to ensure a proper correspondence between the galaxies with IRS spectra and the galaxies with SDSS spectra and end up with 36 objects that are listed in Table 6. Although most galaxies in our *Spitzer* sample are bright enough in the optical to be selected for the main galaxy survey of the SDSS (Strauss et al. 2002), the SDSS observations cover a quarter of the sky whereas the *Spitzer* sample is selected over the entire sky; hence only a third of the objects are matched. Since the SDSS spectroscopic database operates on the vacuum wavelength scale, we use vacuum wavelengths for fits to SDSS data and mark with ‘v’ all such cases in this section.

Because we are interested in the kinematics of the gas relative to the galaxy potential, we start by computing accurate redshifts of the stellar component of the galaxy. To this end, we use absorption features that are due to stellar photospheres. In particular, most spectra show high-order Balmer absorption lines ($v3836.47\text{\AA}$, $v3798.98\text{\AA}$, $v3771.70\text{\AA}$), presumably due to A stars common to these starbursting or post-starbursting objects. If these are not available, or if they are swamped with emission features of ionized interstellar gas, then we use $\text{Ca II } v3934.78\text{\AA}$, but we do not prefer it over the Balmer lines because it may be contaminated by interstellar absorption. When one or more of these absorption lines are detected, we fit them with Gaussians to determine the absorption line centroids, and use median averaging if more than one absorption line is available. In a few cases none of these or other common stellar absorption features are detected and we adopt the SDSS pipeline redshift. Example fits are shown in Figure 2. Whenever we make

kinematic measurements from the SDSS data, we use the accurate stellar redshifts as a reference point.

The majority of objects in our sample show pronounced Na I D absorption due to the cold neutral interstellar medium of the galaxy. To determine the kinematics of this absorption relative to the stellar component of the galaxy, we follow the fitting procedure similar to that suggested by Chen et al. (2010) and Rupke, Veilleux & Sanders (2002). One complication is that there is a He I $v5877.25\text{\AA}$ emission line very close to the relevant wavelength range. It is not a concern for Chen et al. (2010) who pre-subtract weak emission features, whereas we have to perform a simultaneous He I emission / Na I D absorption fit. Emission $I_\lambda(\lambda)$ is described by four parameters: the local continuum and the amplitude, the velocity offset and the velocity dispersion of a Gaussian He I feature. Absorption is described by another four parameters: the covering factor C_f , the peak optical depth τ_0 of the longer wavelength component of the Na D doublet ($\lambda_R = v5897.56\text{\AA}$), the velocity dispersion of the absorbing gas σ_{Na} and its systemic velocity offset v_{Na} . The peak optical depth of the shorter wavelength component ($\lambda_B = v5891.56\text{\AA}$) is set at $2\tau_0$ by the transition probabilities within the relevant levels of the Na atom. Then the model we fit to the data is

$$M_\lambda(\lambda) = I_\lambda(\lambda) \times [1 - C_f + C_f \exp(-\tau_R(\lambda) - \tau_B(\lambda))], \quad (4)$$

where the optical depth of the ‘red’ (longer wavelength) feature is given by

$$\tau_R(\lambda) = \tau_0 \exp \left[-(\lambda - \lambda_R - v_{\text{Na}}\lambda_R/c)^2 / (2(\sigma_{\text{Na}}\lambda_R/c)^2) \right], \quad (5)$$

with the ‘blue’ (shorter wavelength) feature having the same kinematics but twice as high normalization. Example fits are shown in Figure 2.

As discussed by Chen et al. (2010), the covering factor, the peak optical depth and to a lesser extent the velocity dispersion are somewhat degenerate with each other because all three determine the apparent depth of the lines. Since the two components of the doublet are blended with each other, the velocity dispersion measurement relies on the wings of the absorption profile. Furthermore, in a couple of objects the absorption appears to consist of two or more kinematically distinct components. We thus consider the σ_{Na} to be only crude estimates and wherever we report them, we do not correct them for the instrumental resolution of the SDSS spectra ($\sigma_{\text{SDSS}} \simeq 64 \text{ km sec}^{-1}$). To partially mitigate these problems, we construct a more robust physically motivated combination of these parameters, the estimated equivalent width:

$$\text{EEW} \simeq 3\sqrt{2\pi}\sigma_{\text{Na}}\lambda_R\tau_0C_f/c. \quad (6)$$

This value is measured in \AA and for weak lines is approximately equal to the total equivalent width of Na D absorption (the equality is only approximate because this definition of EW uses only the first term of the Taylor expansion in equation 4). The outflow velocity is the most robust measure as long as the stellar redshift is reliable.

We now proceed to the measurements of the kinematics of the ionized gas, where we focus on the $[\text{O III}]\lambda 5007\text{\AA}$ emission. We assume that both components of the $[\text{O III}]\lambda 5007\text{\AA}$ doublet have the same kinematic structure and that the ratio of the peak flux density of the $v4960.3\text{\AA}$ line is fixed at 0.337 relative to the stronger line at $v5008.2\text{\AA}$. We use one to four Gaussian components to produce a good representation of the shape of the line. As these fits are not necessarily unique, we do not attempt to interpret individual components within the line profiles. Rather, we use the fits to obtain non-parametric measures of the kinematics (Whittle 1985;

¹ <http://mirror.sdss3.org/bulkSpectra>

Table 5. Optical spectroscopic measurements from Veilleux, Kim & Sanders (1999)

IRAS Name (1)	$\log \frac{H\alpha}{H\beta}$ (2)	FWHM [O III] (3)	$\log \frac{[O III]}{H\beta}$ (4)	$\log \frac{[N II]}{H\alpha}$ (5)	$\log \frac{[S II]}{H\alpha}$ (6)	$\log \frac{[O I]}{H\alpha}$ (7)
IRAS 00091-0738	0.91	...	-0.37	-0.32	-0.37	-1.54
IRAS 00188-0856	1.17	...	-0.44	0.13	-0.44	-0.93
IRAS 00397-1312	0.86	440.0	-0.53	-0.35	-0.53	-1.28
IRAS 00456-2904	0.80	340.0	-0.47	-0.30	-0.47	-1.41
IRAS 00482-2720	0.97	...	-0.71	-0.18	-0.71	-0.74

Notes. – (1) Object IRAS Name. (2) Flux of $H\alpha$ relative to flux of $H\beta$. (3) Full width at half maximum of $[O III]\lambda 5007\text{\AA}$ in km/s. (4) Logarithm of flux of $[O III]\lambda 5007\text{\AA}$ relative to $H\beta$. (5) Logarithm of flux of $[N II]\lambda 6583\text{\AA}$ relative to $H\alpha$. (6) Logarithm of flux of the sum of $[S II]\lambda\lambda 6716, 6731\text{\AA}$ relative to $H\alpha$. (7) Logarithm of flux of $[O I]\lambda 6300\text{\AA}$ relative to $H\alpha$.
(A full version of this table is available in the online journal.)

Table 6. Optical measurements from the SDSS spectra for a subsample of 36 ULIRGs

IRAS Name (1)	index (2)	SDSS ID (3)	v_{Na} (4)	EEW(NaD) (5)	$v_{02}([OIII])$ (6)	$w_{90}([OIII])$ (7)
IRAS 01166-0844:NW	6	0660-52177-0563	70	2.50	-114	235
IRAS 01572+0009	13	0403-51871-0550	0	0.00	-1661	1845
IRAS 03209-0806	17	0460-51924-0093	-342	5.14	-1284	1289
IRAS 08201+2801	26	1267-52932-0383	-120	1.68	-289	447
IRAS 08559+1053	28	2575-54085-0125	179	5.46	-486	804

Notes. – (1) Object IRAS Name. (2) 0-based index of the object in the *Spitzer* tables. (3) SDSS spectroscopic identification (plate – MJD of observations – fiber). (4) Velocity centroid of the Na D absorption feature relative to the stellar continuum, in km sec^{-1} . (5) Estimated equivalent width of the Na D absorption feature, in \AA . (6) Maximal blueshift of the $[OIII]\lambda 5007\text{\AA}$ emission line relative to the stellar continuum, in km sec^{-1} . (7) Velocity width containing 90 per cent of the $[OIII]$ line power, in km sec^{-1} .
(A full version of this table is available in the online journal.)

Liu et al. 2013b). We calculate the cumulative flux as a function of velocity:

$$\Phi(v) \equiv \int_{-\infty}^v F_v(v') dv', \quad (7)$$

so that the total line flux is $\Phi(\infty)$ and the median velocity is the value at which 50% of line flux accumulates: $\Phi(v_{50}) = 0.5\Phi(\infty)$. Similarly, we can define velocity at 2 per cent, 5 per cent, and 95 per cent cumulative power (v_{02} , v_{05} , v_{95} , etc.). Furthermore, we use the velocity width containing 90 per cent of the line power, $w_{90} \equiv v_{95} - v_{05}$, measured in km sec^{-1} . For a Gaussian profile, this measure would correspond to $1.4\times$ the full width at half maximum. Example fits and non-parametric measures are shown in Figure 3.

Depending on the redshift and specific dataset, the objects in this study may appear point-like or well-resolved on the sky. The datasets all have different apertures which may or may not cover the entire source. In order to avoid any aperture mismatches, we avoid using absolute fluxes from any dataset. In particular, we use line ratios derived from two lines measured from the same dataset (e.g., H_2/PAH ratios, in which both the numerator and the denominator are from *Spitzer* spectra), or equivalent widths, or kinematic measures – in other words, only values that are insensitive to the exact aperture of the observations. Furthermore, in constructing line ratios we try to normalize line fluxes by star formation indicators by placing $H\alpha$, $H\beta$, $\text{Pa } \alpha$ and PAH fluxes in the denominators whenever possible.

3 RELATIONSHIPS BETWEEN WARM H_2 AND GLOBAL PROPERTIES OF ULIRGS

Over a wide range of star formation rates, normal galaxies display a tight relationship between the luminosities of H_2 rotational lines and the luminosities of the PAH features, with only about 0.2 dex variance if the H_2/PAH ratios (Roussel et al. 2007). Since PAH-emitting particles are normally heated by the ultra-violet photons produced by young luminous stars, the strong correlation between PAH and H_2 fluxes indicates that H_2 emission in these objects is also tied to the emission of young stars.

However, this relationship breaks down at the highest galaxy luminosity. The median H_2/PAH ratios in ULIRGs exceed those seen in normal star-forming galaxies by a factor of 3 or more (Zakamska 2010), and ULIRGs no longer show a tight correlation between H_2 and the star-formation indicators. For example, $\log(S(3)/\text{PAH}[11.3\mu\text{m}]) = -1.99 \pm 0.25$ for normal star-forming galaxies in the sample of Smith et al. (2007), but the same ratio is -1.51 ± 0.31 in our sample of ULIRGs. Similarly, in low-luminosity galaxies $\log(S(1)/\text{PAH}[7.7\mu\text{m}]) = -2.48 \pm 0.14$, and the same ratio is -1.91 ± 0.36 among ULIRGs.

Furthermore, H_2 emission appears to be less affected by dust absorption than PAH emission and therefore H_2 emission likely has a more extended spatial distribution by comparison to the bulk of the star formation (Higdon et al. 2006; Zakamska 2010). Using near-infrared ro-vibrational lines, Davies et al. (2003) also find hints that the ratios of H_2 to other lines increase toward the outer parts of the ULIRGs they studied (although in this case, the overall fluxes of H_2 lines are not inconsistent with excitation by ultra-violet photons).

In this section and the next one, we investigate the observed

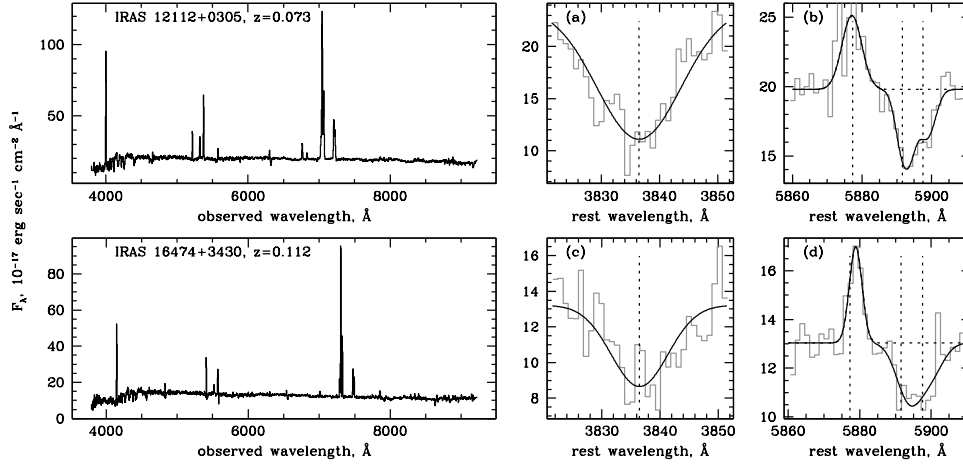


Figure 2. Left: Example optical spectra of two ULIRGs in our sample from the SDSS database. Middle and right: Fits to stellar Balmer absorption features (panels a and c) and to the He I emission and Na D doublet absorption (panels b and d) in the same two objects (IRAS 12112+0306 and IRAS 16474+3430). Vertical dashed lines show the laboratory wavelengths of the features in question. The rest wavelengths are determined by finding accurate centroids of Balmer absorption features (in this case, H9 or H γ with vacuum wavelength 3936.47 Å); thus, in panels a and c the Gaussian fits are centered on their laboratory values by design. In the He I / Na D fits velocity offsets are allowed.

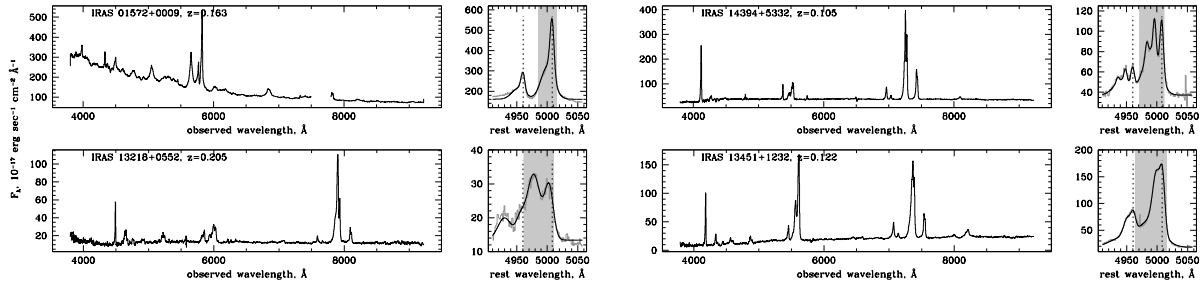


Figure 3. Overall optical spectra and multi-Gaussian fits to the [OIII] $\lambda\lambda$ 4960.3,v5008.2 Å doublet in the four objects with the largest [OIII] velocity width. Dashed lines mark the laboratory wavelengths of the components of the doublet in the rest-frame of the galaxy as determined by stellar absorption features; in all four objects most of the line flux is blue-shifted relative to the expected wavelength. Shaded regions mark the range of velocities that encloses 90 per cent of the line flux, from v_{05} to v_{95} , in each object. All four objects contain a powerful active nucleus. The alternate names and classifications from the NASA Extragalactic Database are: Mrk 1014 – quasar (for IRAS 01572+0009; data are missing between 7500 and 7800 Å), quasar (for IRAS 13218+0552), Seyfert 2 galaxy (for IRAS 14394+5332), 4C +12.50 – Seyfert 1 galaxy (for IRAS 13451+1232).

relationships between the amount of H₂ emission and other properties of ULIRGs in order to determine the origin of this excess emission. In most cases we use the H₂/PAH ratios to quantify the excess of H₂ over that expected the star formation rates.

3.1 Effects of an active nucleus

We first investigate whether the presence of an AGN affects the H₂/PAH ratios. As the first step, following Yuan, Kewley & Sanders (2010), we split the sample into four subsamples by optical classification: purely star-forming objects whose spectra are consistent with those of HII regions (13 objects), AGNs (37 objects, combining type 1 and type 2 objects), and star formation / AGN composites (53 objects). We use the KS test to determine whether any two of these subsamples show statistically different distributions of H₂/PAH or T_{exc} .

We find that galaxies classified as AGNs or composites have slightly higher S(3)/PAH[11.3 μ m] emission than star-forming galaxies (Figure 4, left), which is similar to the trends seen in lower luminosity galaxies (Rigopoulou et al. 2002; Roussel et al. 2007). Star-forming galaxies have a median

$\log(\text{S}(3)/\text{PAH}[11.3 \mu\text{m}]) = -1.83 \pm 0.32$. Composite galaxies have median $\log(\text{S}(3)/\text{PAH}[11.3 \mu\text{m}]) = -1.54 \pm 0.28$ ($p_{\text{KS}} = 0.064$ between this population and the star-forming galaxies). Galaxies classified as AGNs have median $\log(\text{S}(3)/\text{PAH}[11.3 \mu\text{m}]) = -1.43 \pm 0.32$ ($p_{\text{KS}} = 0.044$ between active nuclei and star-forming galaxies). Thus there is a general, albeit weak, trend that the H₂/PAH ratios increase as the fractional contribution of the active nucleus to the optical diagnostics increases. The median excitation temperature measured from the S(3)-S(1) transition is 406 K. We do not see any difference in T_{exc} between galaxies of different optical classification.

Optical emission lines are not necessarily the most reliable diagnostic of the presence of an active nucleus in objects that are heavily obscured by dust. Furthermore, because of the sensitivity of optical diagnostics to the spatial distribution of dust extinction they cannot be used to determine the relative contributions of the star formation and of the accretion onto a supermassive black hole to the bolometric luminosity of ULIRGs. Mid-infrared diagnostics are less affected by obscuration and thus may be more reliable. In particular, the equivalent widths of the PAH features can serve as a measure of the contribution of the active nucleus to the total energy

budget of a ULIRG (Imanishi & Dudley 2000; Armus et al. 2007; Spoon et al. 2007). Indeed, the luminosity of the PAH features is a good indicator of star-formation rates (Roussel et al. 2001; Dale & Helou 2002), whereas the continuum is produced by dust heated both by star formation and the active nucleus. Thus, low equivalent widths of PAH emission are expected in objects powered predominantly by black hole accretion. The equivalent width of the $6.2\mu\text{m}$ PAH feature is a particularly good indicator. The active nucleus, if any, makes a two-fold contribution: it dominates the continuum at these short wavelengths (and correspondingly warmer dust temperatures) and it suppresses the emission of the feature itself (Diamond-Stanic & Rieke 2010).

We find an anti-correlation between $S(3)/\text{PAH}[11.3\mu\text{m}]$ and the equivalent width of the $\text{PAH}[6.2\mu\text{m}]$ feature ($p_S = 3 \times 10^{-6}$; Figure 4, right). Thus the mid-infrared data indicate that the presence of an active nucleus is either associated with the destruction of the $\text{PAH}[6.2\mu\text{m}]$ emission, as was suggested by Smith et al. (2007) and Diamond-Stanic & Rieke (2010), or with production of excess H_2 , or both. We do not see any relationship between T_{exc} and $\text{PAH}[6.2\mu\text{m}]$ equivalent width.

There are some drawbacks to using equivalent widths of PAHs as the measure of the AGN contribution. For example, low equivalent width of PAHs can be due to low metallicity rather than high AGN contribution, and the lack of excitation of PAHs by emission from active nuclei is not well understood (Farrah et al. 2007 provide a detailed discussion). Furthermore, in Figure 4 PAH luminosities (albeit of two different features) appear both in the numerator of the horizontal axis and the denominator of the vertical axis, which could potentially give rise to a spurious anti-correlation. Thus, we examine the relationships between $S(3)/\text{PAH}[11.3\mu\text{m}]$ and other measures of AGN activity suggested in the literature, especially ones based on high-ionization emission lines (Farrah et al. 2007). In particular, we find that $S(3)/\text{PAH}[11.3\mu\text{m}]$ positively correlates with $[\text{Ne V}]\lambda 14.32\mu\text{m}/[\text{Ne II}]\lambda 12.81\mu\text{m}$ ($p_S = 10^{-4}$), confirming our finding that excess H_2 is more pronounced in objects with stronger AGN activity. Objects with higher $S(3)/\text{PAH}[11.3\mu\text{m}]$ tend to have higher $[\text{O IV}]\lambda 25.89\text{\AA}/[\text{Ne II}]\lambda 12.81\mu\text{m}$ ratios as well, but the correlation is marginal at best ($p_S = 0.1$). The main drawback to using these diagnostics is that $[\text{Ne V}]\lambda 14.32\mu\text{m}$ and $[\text{O IV}]\lambda 25.89\text{\AA}$ are reliably measured in only 20-30 of our sources.

To summarize, we use a variety of optical and infrared diagnostics to test the relationship between the excess H_2 and the presence of AGN activity. While none of the diagnostics provides a perfect measure of the AGN contribution to the overall energetics, in all cases we see a trend of higher H_2/PAH ratios in objects with stronger AGN activity.

3.2 Effects of galaxy morphology and merger stage

Numerical simulations have shown that major galaxy mergers are able to induce nuclear gas flows and produce strong starburst episodes (Barnes & Hernquist 1991, 1996; Mihos & Hernquist 1996, 1994). The nuclear gas inflows during the merger sequence are due to the strong non-axisymmetric perturbations in the gravitational potential induced by each galaxy on its companion. While the gas may have started in rotational equilibrium within each galaxy disk, the non-axisymmetric potential induced during the merger results in the appearance of radial orbits which do not conserve angular momentum and funnel the gas toward the centre of the galaxy (Binney & Tremaine 2008), where it compresses, shocks and gives rise to new stars. The same non-axisymmetric potential that pro-

motes the driving of gas into the nuclear region of the galaxy also promotes the development of long tidal tails (Barnes & Hernquist 1991).

Tracing of these phenomena throughout the merger (Narayanan et al. 2010a,b; Torrey et al. 2012) gives insight into the timing of these events. After the first close passage, nuclear mass inflow and the resulting star formation rate increase steadily for ~ 100 Myr and remain fairly high while the galaxies conduct their quasi-Keplerian orbital motion around each other, moving out to the apo-galacticon (which can be many tens of kpc) and coming back for the second close approach.

Because gas-rich galaxy mergers are dissipative, the second close approach tends to be closer than the first one, and subsequently the galaxies separate by only a few kpc for only a short period of time before the final coalescence. The typical time scale for the entire merger from the first approach to the final coalescence is on the order of 1 Gyr, with 90 per cent of it taken by the time between the first and the second close passage (Torrey et al. 2012). The gas inflow rate and the star formation rate peak strongly between the second close approach and the final coalescence, but for a relatively short period (0.1 Gyr; Narayanan et al. 2010a,b; Torrey et al. 2012).

ULIRGs are defined by their high infrared luminosity, which is largely due to a very high star formation rate, and thus it is not surprising to find the vast majority of ULIRGs in merging systems (Sanders & Mirabel 1996). Given the importance of the merger process in the development of ULIRGs, we look for possible connections between H_2 and morphological features associated with merger activity. We do not find any differences in the distribution of H_2/PAH between the Pre-Merger, Merger and Old Merger classes ($p_{\text{KS}} = 0.2 - 0.4$; Figure 5) nor do we see a difference in the distribution of T_{exc} between any merger classes ($p_{\text{KS}} = 0.3 - 0.9$). Thus we do not confirm the trend seen by Petric et al. (2010) who find higher excitation temperatures of H_2 in advanced mergers within a somewhat less luminous sample of galaxies (Petric et al. 2011).

Within the Pre-Merger class, the easily measurable apparent nuclear separation does not yield a direct measure of merger progress: the approaching galaxies on first approach, the receding galaxies right past the first approach on the way to apo-galacticon and the approaching galaxies on the way to the second approach could all have the same nuclear separation, although after the second approach the merging pairs do not tend to separate much (Torrey et al. 2012). Furthermore, projection effects make it difficult to distinguish widely separated galaxies which happen to be close to the line of sight from pairs at smaller physical separations. Nevertheless, in a large unbiased survey of galaxy pairs the apparent nuclear separation correlates with the excess star formation rate induced during the interaction (Ellison et al. 2013). Thus the apparent nuclear separation must provide some measure of the interaction stage.

We do not find any correlation between $S(3)/\text{PAH}[11.3\mu\text{m}]$ and projected nuclear separation ($p_S = 0.99$) nor between excitation temperature T_{exc} and projected nuclear separation ($p_S = 0.95$). We previously hypothesized that shocks produced directly in the galaxy collisions could be responsible for the excess H_2 observed in ULIRGs (Zakamska 2010), by analogy to other systems in which high-velocity intra-group collisions are associated with warm H_2 emission (Appleton et al. 2006; Peterson et al. 2012; Cluver et al. 2013); our new results indicate that this hypothesis is an unlikely explanation. Indeed, one would expect to see the strongest effect of galaxy collision shocks in pairs with smallest nuclear separations or in the Merger class.

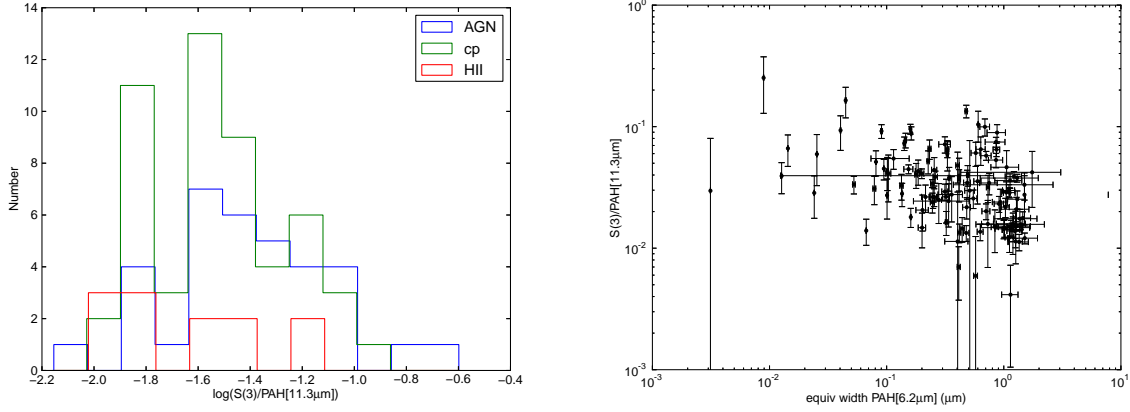


Figure 4. **Left:** The distributions of H_2/PAH ratios by optical classification. We see slightly higher $\text{S}(3)/\text{PAH}[11.3\mu\text{m}]$ ratios in galaxies classified as AGNs or star-formation/AGN composites than in purely star-forming galaxies ($p_{\text{KS}} = 0.04$ and $p_{\text{KS}} = 0.064$, respectively). **Right:** We find an anti-correlation between $\text{S}(3)/\text{PAH}[11.3\mu\text{m}]$ and equivalent width of $\text{PAH}[6.2\mu\text{m}]$ ($p_{\text{S}} = 3 \times 10^{-6}$) indicating that H_2 excess is stronger in galaxies with a larger relative contribution of the active nucleus. (For comparison, the median value of $\text{S}(3)/\text{PAH}[11.3\mu\text{m}]$ in low-luminosity star-forming galaxies is 0.01, below most values found in our sample of ULIGRs.)

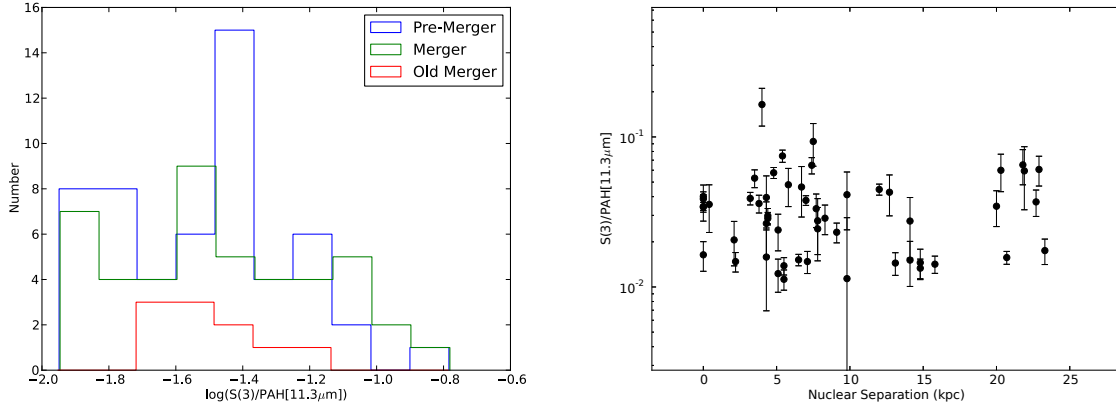


Figure 5. **Left:** $\text{S}(3)/\text{PAH}[11.3\mu\text{m}]$ is constant across merger class ($p_{\text{KS}} = 0.2 - 0.4$ between any pair of categories). **Right:** $\text{S}(3)/\text{PAH}[11.3\mu\text{m}]$ is uncorrelated with projected nuclear separation ($p_{\text{S}} > 0.9$).

Tidal tails are another useful feature in determining the stage of the merger. The production of tidal tails is dependent on the collision geometry with the longest tidal tails developing in collisions where there is a resonance in rotational motion in prograde encounters (Toomre & Toomre 1972). In general, tidal tail length monotonically increases as a function of time, although again the projection effects and the disappearance of features as they fall below the surface brightness detection threshold make it difficult to use them as a precise timer of the merger. We do find an association between the length of the tidal tails in our objects and excess H_2 emission ($p_{\text{S}} = 0.01$) as well as a more tentative association with T_{exc} ($p_{\text{S}} = 0.04$; Figure 6). Pure star formation galaxies tend to have tidal tails less frequently (2 of 13, 15 per cent) compared to composites (34 of 53, 64 per cent) and active nuclei (24 of 37, 65 per cent). However, there is no correlation between tidal tail length and the equivalent width of $\text{PAH}[6.2\mu\text{m}]$ – a measure of the AGN contribution.

For the 36 objects with the SDSS spectra, we estimate the age of the starburst by using the strength of the 4000\AA break

(Kauffmann et al. 2003) which is parametrized by the ratio of average flux densities on either side of the break, $D_n(4000) = \langle f_{\nu}(4000 - 4100) \rangle / \langle f_{\nu}(3850 - 3950) \rangle$. As a stellar population ages and becomes redder, the value $D_n(4000)$ monotonically increases; the precise calibration of this parameter with starburst age is presented by Kauffmann et al. (2003). Before this value can be measured, the emission lines need to be subtracted to reveal the pure stellar continuum of the galaxy. In our objects, a particularly strong line in the relevant wavelength range is $[\text{Ne III}]\lambda 3870\text{\AA}$, which we either interpolate over using surrounding continuum or exclude from the calculation of $\langle f_{\nu}(3850 - 3950) \rangle$ entirely – the results are insensitive to the specific procedure used.

We find that $D_n(4000)$ values range between 1.0 and 1.6, corresponding to starburst ages between $\tau_{\text{SB}} = 10$ Myr and 1 Gyr. The median and the standard deviation of $D_n(4000)$ is 1.20 ± 0.14 , corresponding to the median age $\tau_{\text{SB}} = 250$ Myr. We find no correlation between $\text{S}(3)/\text{PAH}[11.3\mu\text{m}]$ and the age of the starburst ($p_{\text{S}} > 0.08$), and within the range of starburst ages in our sample there is no particular value associated with stronger H_2 emission.

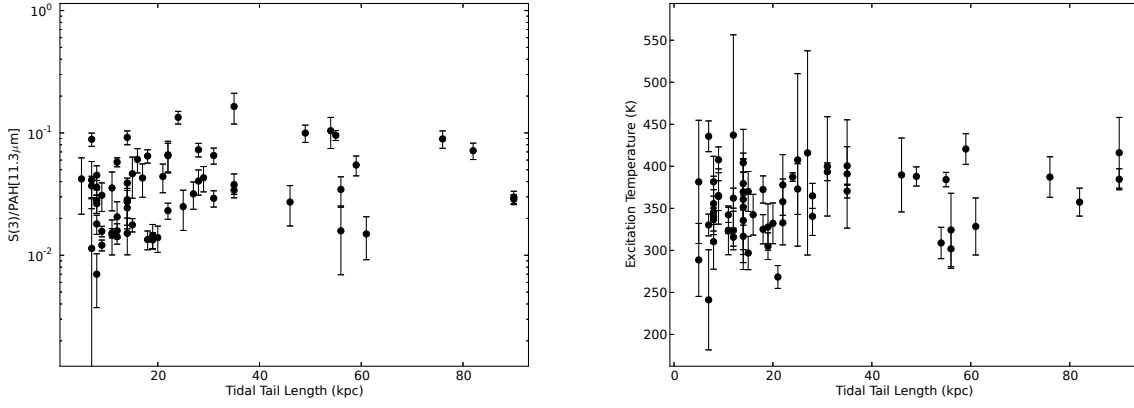


Figure 6. The length of tidal tails correlates weakly with $S(3)/PAH[11.3\mu m]$ (left, $p_S = 0.01$) as well as with T_{exc} (right, $p_S = 0.04$).

To summarize, objects with strongest excess H_2 emission do not have preference for a specific merger stage or starburst age. However, the correlation with the tidal tail length indicates that the amount of excess H_2 emission and the excitation temperature increase with time during galaxies' orbit after the first close approach.

4 RELATIONSHIP BETWEEN WARM H_2 AND OTHER GAS PHASES

The interstellar medium of a normal galaxy is comprised of gas at a wide range of densities and temperatures. Each phase of this medium produces its own emission and absorption depending on the dominant radiative processes in this phase. In this section, we use the rotational lines of H_2 to probe the warm molecular gas phase of the interstellar medium; optical, near-infrared and mid-infrared recombination emission lines to probe the ionized gas phase; and the Na D doublet to probe the neutral gas phase. Using these diagnostics, we investigate the relationships between the kinematics and the physical conditions of gas in these three phases.

4.1 Optical lines of ionized and neutral gas

Optical emission lines produced by ionized and neutral gas carry information about the physical conditions in the gas and its source of ionization and excitation. We start by looking at the correlations between H_2/PAH and the optical line ratios, such as $[N II]\lambda 6583\text{\AA}/H\alpha$, $[O I]\lambda 6300\text{\AA}/H\alpha$, $[S II]\lambda\lambda 6716, 6731\text{\AA}/H\alpha$ and $[O III]\lambda 5007\text{\AA}/H\beta$. The combination of these measurements can be used to determine gas metallicity, ionization parameter, and relative strengths of the contributions of shock- and photo-ionization. We find a positive correlation between $S(3)/PAH[11.3\mu m]$ and $[OI]/H\alpha$ ($p_S = 10^{-8}$, Figure 7), but weaker, if any, correlations between $S(3)/PAH[11.3\mu m]$ and the other ratios: $p_S = 0.03$ for $[N II]\lambda 6583\text{\AA}/H\alpha$, $p_S = 10^{-3}$ for $[S II]\lambda\lambda 6716, 6731\text{\AA}/H\alpha$, and $p_S = 2 \times 10^{-3}$ for $[O III]\lambda 5007\text{\AA}/H\beta$.

The relative strengths of these correlations – in particular, the fact that the strongest correlation is with $[O I]\lambda 6300\text{\AA}/H\alpha$ – suggest that the H_2/PAH ratios are driven in large part by the relative contribution of shocks. Indeed, while all these four optical line ratios increase as the fractional contribution of shocks increases, the $[O I]\lambda 6300\text{\AA}/H\alpha$ ratio has the strongest sensitivity on the shock fraction. As shown by Rich, Kewley & Dopita (2011), at a fixed

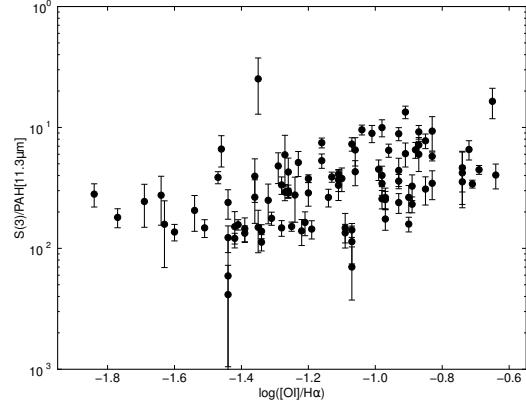


Figure 7. We look at the relationships between H_2/PAH and optical line ratios, such as $[O I]\lambda 6300\text{\AA}/H\alpha$, $[N II]\lambda\lambda 6583\text{\AA}/H\alpha$, $[S II]\lambda\lambda 6716, 6731\text{\AA}/H\alpha$, and $[O III]\lambda 5007\text{\AA}/H\beta$. The strongest correlation is between $S(3)/PAH[11.3\mu m]$ and $[O I]\lambda 6300\text{\AA}/H\alpha$ ($p_S = 10^{-8}$) shown here.

ionization parameter, increasing the shock contribution to gas ionization from 5 per cent to 80 per cent increases $[O III]\lambda 5007\text{\AA}/H\beta$ by ~ 0.4 dex, $[S II]\lambda\lambda 6716, 6731\text{\AA}/H\alpha$ and $[N II]\lambda 6583\text{\AA}/H\alpha$ by ~ 0.8 dex, and $[O I]\lambda 6300\text{\AA}/H\alpha$ by ~ 1.2 dex. The values of $[O I]\lambda 6300\text{\AA}/H\alpha$ that we see in our sample span the entire range of models probed by these authors.

Conversely, at a fixed shock fraction the $[O I]\lambda 6300\text{\AA}/H\alpha$ line ratio is the least sensitive to the variations in the ionization parameter. If H_2/PAH variations among the objects in our sample were driven by the variations in the ionization parameter, we would expect a weaker, if any, correlation with $[O I]\lambda 6300\text{\AA}/H\alpha$ than with the other line ratios. Thus, although AGNs have somewhat higher H_2/PAH ratios (as we saw in Sec. 3.1), the mere presence of an AGN or even its fractional contribution to the ionization balance do not appear to be the primary driving factors for the amount of H_2 emission. This conclusion is similar to that reached by Roussel et al. (2007) who considered excess rotational H_2 emission in lower-luminosity galaxies. These authors also found that direct excitation by the emission from an AGN (specifically, by the

X-rays from the AGN) is insufficient to produce the observed excess of H_2 .

Relationships between the kinematics of the ionized gas and the $\text{S}(3)/\text{PAH}[11.3\mu\text{m}]$ ratios offer further clues regarding the origin of the H_2 emission in ULIRGs. We find a positive correlation between $\text{S}(3)/\text{PAH}[11.3\mu\text{m}]$ and the velocity widths of the optical emission lines (Figure 8). The correlation is present both when we consider the single-Gaussian fits to low-resolution spectroscopic data and when we perform the multi-Gaussian fitting more sensitive to weak broad components in emission lines. There is no correlation between the excitation temperature of H_2 and optical line widths.

Like many other authors (e.g., Soto et al. 2012), we find that the optical emission line gas shows predominantly blue-shifted asymmetries (e.g., Figure 3). Taken by itself, this observation indicates that the ionized gas in ULIRGs is likely embedded in an outflow, which may be intrinsically symmetric, but its redshifted part (being located on the other side of the galaxy from the observer) is dimmed by the intervening galaxy material. Furthermore, in ULIRGs there is a strong correlation between the line-of-sight velocity dispersion of the ionized gas and the shock contribution to its ionization balance (Rich, Kewley & Dopita 2011; Soto et al. 2012). This likely means that higher outflow velocities (reflected in the line-of-sight velocity dispersion) produce stronger shocks which are more likely to ionize the clouds they impact.

As already mentioned in Sec. 3, we do not see any correlations between H_2/PAH and the ages of the stellar populations (as measured by $D_n(4000)$); neither do we find one between the velocity of the outflow (as measured either by v_{02} or by w_{90}) and the ages of the stellar populations. Thus there is no particular age of the stellar populations when the outflows have highest velocity. This is likely a result of the long duration of the starburst induced on the initial approach. Because gas is continually supplied throughout the merging process, the $D_n(4000)$ is unlikely to be a particularly accurate clock of the merger.

The relationships between excess H_2 emission, optical line ratios and optical line kinematics suggest a picture in which a galaxy-wide outflow that shocks and entrains the interstellar medium is responsible for some of the optical line emission as well as much of the warm H_2 emission. Stronger shocks appear to be associated with higher outflow velocities and stronger H_2 emission.

What is the origin of these outflows? Most of them are likely driven by explosions of supernovae associated with the recent star formation activity (Soto et al. 2012). But while the majority of the ULIRGs are likely powered by high rates of star formation, the four objects with the largest $[\text{O III}]\lambda 5007\text{\AA}$ velocity widths in our sample (Figure 3) are all optically classified as AGNs, one of them radio-loud. How do AGNs affect the excitation of H_2 ? Roussel et al. (2007) find that X-rays are in general insufficient to explain the excess H_2/PAH ratios in nearby low-luminosity galaxies. Therefore, given the correlation between H_2 and $[\text{O III}]\lambda 5007\text{\AA}$ emission line width in our sample, we propose that H_2 emission in all ULIRGs is dominated by shocks, both in starburst-dominated objects (where the winds are driven by supernovae explosions) and in the AGN-dominated ones (Diamond-Stanic & Rieke 2010). In the latter case, the outflow may be driven either by the relativistic jets or by the radiation pressure due to the accretion onto the supermassive black hole (Murray et al. 1995; Proga, Stone & Kallman 2000).

Rupke, Veilleux & Sanders (2005) and Rupke & Veilleux (2013) suggest that outflow velocity can be used as a discriminant of starburst-driven vs AGN-driven winds. Using the highest

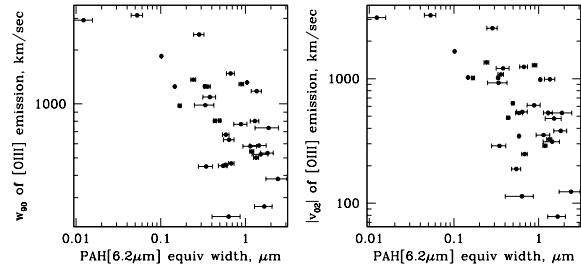


Figure 9. Two different measures of wind velocity as a function of the contribution of the active nucleus to the bolometric luminosity strongly correlate with the equivalent width of $\text{PAH}[6.2\mu\text{m}]$ ($p_S = 2 \times 10^{-4}$ and 6×10^{-5}) which serves as an indicator of the AGN contribution to the bolometric luminosity. An object powered by an AGN and by star formation in roughly equal measures has $\text{EW}(\text{PAH}[6.2\mu\text{m}])$ of about $0.3\mu\text{m}$ (Armus et al. 2007). Thus objects on the left-hand side of each panel are AGN-dominated and those on the right-hand side are star-formation-dominated.

blueshifted velocity (in our notation it is the velocity at the 2 per cent of the line flux v_{02}), they find median values of $v_{02} \simeq -1000 \text{ km sec}^{-1}$ for AGN-driven winds and -500 km sec^{-1} for starburst-driven ones. We explore this dichotomy further using the 36 objects with the SDSS spectra in our sample. In Figure 9, we show the outflow velocity – parametrized both by the line width w_{90} and the maximum blueshift velocity v_{02} – as a function of the equivalent width of the $\text{PAH}[6.2\mu\text{m}]$ emission used as a measure of the AGN contribution to the bolometric luminosity.

The AGN-dominated objects on the left-hand side of each panel show significantly higher outflow velocities by both measures than the starburst-dominated objects on the right. The characteristic values we obtain for v_{02} are in agreement with those found by Rupke & Veilleux (2013). Thus it appears likely that the objects with the highest $[\text{O III}]\lambda 5007\text{\AA}$ outflow velocities and velocity widths – which also tend to show high H_2/PAH ratios – have winds driven by the AGN activity. Because of the obscuration of the central AGN, these winds would not necessarily be photoionized (Soto et al. 2012) with characteristic AGN-like line ratios, but would be shock-ionized just like supernova-driven winds. Aside from the buried energy source – supernova explosions vs radiative pressure – the physics of galaxy-wide starburst-driven and AGN-driven outflows is apparently similar.

The observed striking difference in outflow velocities between AGN-dominated and star-formation-dominated ULIRGs has the potential to become a useful diagnostic of the powering source of the outflows. Qualitatively, this velocity difference was predicted in numerical simulations of mergers by Narayanan et al. (2008). In these simulations, the relatively high velocities of AGN-driven outflows are explained by a higher rate of energy injection into the outflow compared to the supernova-driven winds, even though the AGN-dominated phase may be comparatively shorter. Further numerical work will help determine whether the model velocity profiles of emission lines are consistent with those observed.

Our conclusion regarding the origin of H_2 emission in AGNs is somewhat different from that reached by several other groups. Mouri et al. (1989) argue that X-ray emission is likely the dominant source of excitation of ro-vibrational H_2 lines, and Rigopoulou et al. (2002) suggest the same for the rotational H_2 lines, although Roussel et al. (2007) find X-ray emission insufficient

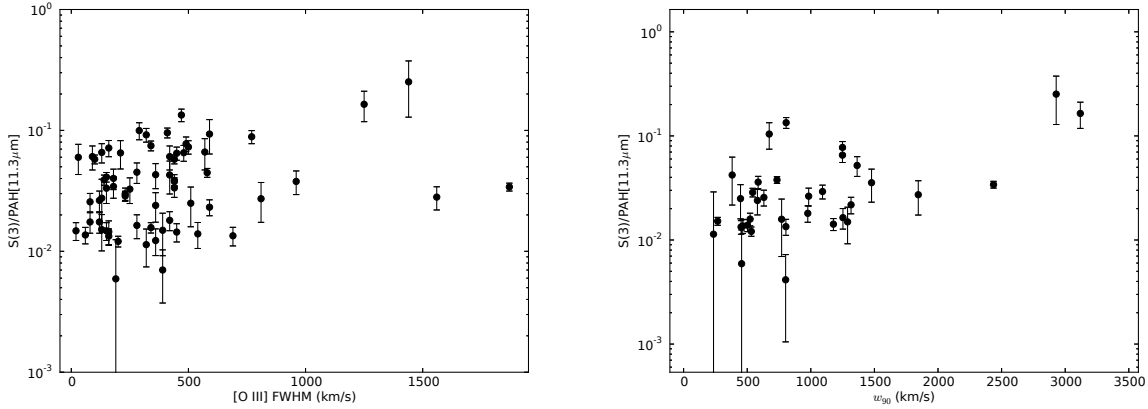


Figure 8. Left: The relationship between $S(3)/PAH[11.3\mu m]$ and the full width at half maximum of $[O III]\lambda 5007\text{\AA}$ taken from Veilleux, Kim & Sanders (1999) for the full sample shows a tentative positive correlation ($p_S = 0.03$). **Right:** The relationship between $S(3)/PAH[11.3\mu m]$ and the velocity widths comprising 90 per cent flux w_{90} for the subsample of 36 objects with SDSS spectra shows a positive correlation ($p_S = 0.002$).

and suggest that starburst-driven winds of the host galaxy provide the H_2 excitation. The luminosity of the AGN appears to be the determining factor of whether it shows a large galaxy-wide outflow (Liu et al. 2013a), with only the most luminous obscured quasars routinely displaying one. The objects that we consider in this paper are much more luminous than those of Mouri et al. (1989), Rigopoulou et al. (2002) and Roussel et al. (2007) – indeed, if the AGN dominates the bolometric luminosity of a ULIRG then it is comparable to the objects studied in Liu et al. 2013a. This significant step up in luminosity may explain why we see the signatures of AGN-driven winds not apparent in the previous samples.

4.2 [Fe II] emission

We find a particularly strong relationship between warm H_2 and [Fe II] emission (Figure 10). We use the near-infrared measurements of $[Fe II]\lambda 1.644\mu m$ by Veilleux, Sanders & Kim (1997) when available and our own measurements of $[Fe II]\lambda 5.34\mu m$ in the mid-infrared made from the *Spitzer* spectra. For the 10 objects with $[Fe II]\lambda 1.644\mu m$ measurements we see a tentative correlation between $[Fe II]\lambda 1.644\mu m/Pa\alpha$ and $S(3)/PAH[11.3\mu m]$. In the mid-infrared, with many more objects we see a much stronger correlation between $[Fe II]\lambda 5.34\mu m$ and $S(3)$ luminosity. Because both line luminosities are derived from the same *Spitzer* spectra, we do not have to normalize the lines in this case.

Furthermore, star-forming objects, those dominated by an AGN and composite galaxies all lie on the same [Fe II]- H_2 sequence, although as we previously established AGNs tend to lie toward its upper end. Strong [Fe II] emission is usually associated with shocks driven into a neutral medium, when they destroy dust grains and release iron into the gaseous phase. The [Fe II] emission is then excited largely by collisions in the post-shock recombination region (Mouri, Kawara & Taniguchi 2000) or by the interstellar radiation field. These conditions are common in supernova remnants: as the effects of many exploding supernovae compound each other, a bubble of hot gas forms and expands as a wind driving shocks into the neutral gas. Near-infrared transitions of [Fe II] provide an accurate measure of supernova rate in starburst galaxies (Morel, Doyon & St-Louis 2002; Rosenberg, van der Werf & Israel 2012), and $[Fe II]\lambda 5.34\mu m$ is expected to be as strong as or stronger than the $[Fe II]\lambda 1.644\mu m$ in su-

pernova remnants (Reach et al. 2006). Thus, the strong correlation between H_2 and [Fe II] in starburst-dominated galaxies confirms that H_2 in these objects is produced in supernova-driven shocks.

The origin of [Fe II] emission in galaxies containing AGNs is more controversial. Moorwood & Oliva (1988) argue that in composite galaxies [Fe II] emission is likely to be dominated by supernova-driven shocks in the host galaxy. Mouri, Kawara & Taniguchi (2000) demonstrate that in low-luminosity AGNs, the X-rays from the nuclei dominate excitation of [Fe II] over any AGN-driven outflows. However, in our case both H_2 and [Fe II] clearly share similar physical origins, and in the previous section we made the case for AGN-driven winds as the origin of galaxy-wide shocks. We suggest that winds – whether driven by the starbursts or by the AGNs – are responsible for shocks that emit both the rotational H_2 lines and the [Fe II] lines in ULIRGs and that these shocked winds dominate over other sources of excitation for the very luminous AGNs and starbursts studied here.

This view is supported by the good correlations between H_2 , $[Fe II]\lambda 5.34\mu m$ and $[O I]\lambda 6300\text{\AA}/H\alpha$ and the poor correlation between H_2/PAH and $[N II]\lambda 6583\text{\AA}/H\alpha$, reminiscent of the relationships found by (Mouri, Kawara & Taniguchi 2000). These authors argue that [Fe II] and $[O I]\lambda 6300\text{\AA}$ are all produced in partly ionized regions, whereas $[N II]\lambda 6583\text{\AA}$ comes from fully ionized gas. Therefore, [Fe II] and $[O I]\lambda 6300\text{\AA}$ are unlikely to be co-spatial with $[N II]\lambda 6583\text{\AA}$ and $[O III]\lambda 5007\text{\AA}$, explaining the weakness of the correlations between these values. Thus the driving mechanism of the wind is not as important as the physical conditions of the medium it is driven into; as long as the gas is dense and neutral enough, it will yield $[O I]\lambda 6300\text{\AA}$, [Fe II] and apparently H_2 emission in the post-shock region.

4.3 Neutral phase

Na I D absorption is much stronger in ULIRGs than it is in normal star forming galaxies. The median EEW(NaD) is 5.3\AA for those of the objects in our sample that have SDSS spectra; for comparison, normal SDSS galaxies with $EW(NaD) > 0.8\text{\AA}$ are considered strong Na D absorbers (Chen et al. 2010). Although some Na D absorption may arise in the atmospheres of cool stars – this effect contributes up to 80 per cent of the Na D equivalent width in normal galaxies – the much higher strength of the absorption in ULIRGs

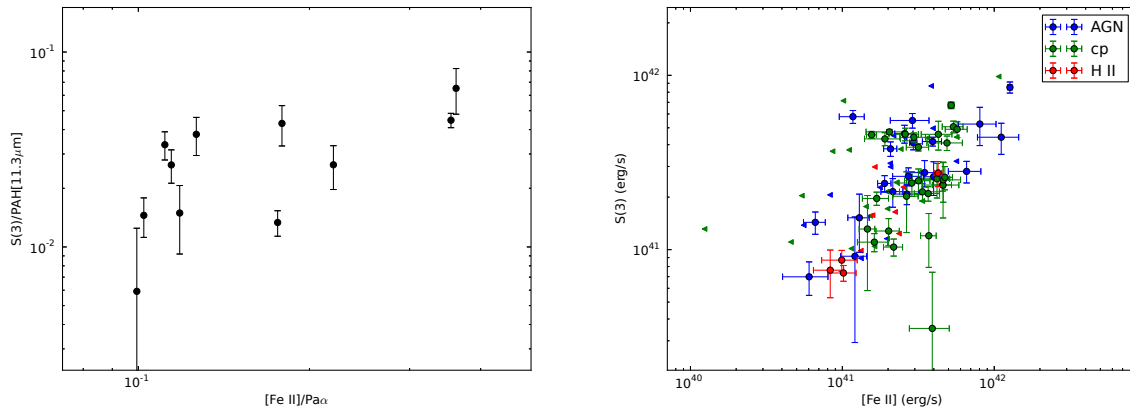


Figure 10. Left: $S(3)/PAH[11.3\mu m]$ and $[Fe II]\lambda 1.644\mu m/P\alpha$ are positively correlated ($p_S = 0.009$), although because of the weakness of $[Fe II]\lambda 1.644\mu m$ the data are available only for 10 objects. Right: $S(3)$ and $[Fe II]$ fluxes are linearly proportional to one another. The plot includes 58 $[Fe II]$ detections at $> 3\sigma$ level (circles) and 44 3σ upper limits (triangles). $p_S = 3.8 \times 10^{-5}$ for detections, $p_S = 4.5 \times 10^{-9}$ for the full set.

implies that the stellar contribution is negligible compared to the interstellar one in our sources.

Chen et al. (2010) demonstrate that in normal disk galaxies there are two components to the Na D absorption. One is at the redshift of the galaxy; it is associated with the rotationally supported gaseous disk and is more likely to be seen when the galaxy is edge-on. The other one is blue-shifted and associated with the galactic outflows; it is more likely seen when the galaxy is pole-on. The signal-to-noise and the spectral resolution of our data do not allow us to decompose Na D into these two components, but we find an anti-correlation between EEW(NaD) and its velocity centroid v_{Na} ($p_S = 0.004$; Figure 11), indicating that the strongest absorption is associated with the largest blue-shifts. Thus, the strongest Na D absorption in our sample is associated with the outflow component. In contrast to Chen et al. (2010), we do not find any correlations between any of the parameters of Na D absorption and galaxy orientation as measured by the apparent ellipticity (taken from Veilleux, Kim & Sanders 2002). This disagreement can be explained if the starbursts – and their associated winds – in ULIRGs are compact and concentrated on scales much smaller than those probed by overall galaxy ellipticities. Alternatively, the correlation may not be detected because we are unable to isolate disk-associated and outflow-associated components separately.

We do not find any strong correlations between H_2 , its T_{exc} and any of the parameters of the Na D absorption. The strongest trend is between $S(3)/PAH[7.7\mu m]$ and EEW(NaD), with $p_S = 0.08$ (i.e., only tentatively detected; Figure 11), in the sense that stronger H_2 excess is associated with objects with weaker Na D absorption. This is a puzzling and counter-intuitive result that suggests that perhaps the same shocks that lead to excess H_2 emission eliminate the regions of the interstellar medium where Na D absorption is produced. A larger sample with better quality data for Na D absorption will lead to a more conclusive result on the relationship between the neutral and the warm molecular phases.

In contrast, the kinematics of the ionized gas and the neutral gas phases are unambiguously correlated. Indeed, high outflow velocities in the neutral component are associated with high outflow velocities in the ionized component ($p_S \gtrsim 0.001$, depending on the exact kinematic measures used). Thus, in the objects with the largest blue-shifts both Na D absorption and ionized gas emission

arise in the same outflow (which presumably consists of pockets of gas with different physical conditions).

Finally, we look at the relationships between various measures of dust extinction. The ones available to us are $\tau[9.7\mu m]$ which can be used as a measure of dust obscuration toward the source of the bolometric power; the Balmer ratio $H\alpha/H\beta$ which can be used as a measure of dust reddening toward the ionized gas; and EEW(NaD) which measures the column density of cold neutral material toward the stellar component of the galaxy and thus in principle should be an indirect measure of dust absorption toward that source. Surprisingly, although all these values are in principle direct or indirect measures of the column density of dust, no two measures are correlated with one another. This likely reflects the complex geometry of ULIRGs, in which the powering source, the ionized gas and the stellar component might all be distributed over very different physical scales.

We conclude that the three phases of the interstellar medium of ULIRGs that we can probe with our data (warm molecular, cold neutral and ionized) are clearly related to one another, but there is no simple relationship between them. On the one hand, the kinematics of Na D and the [OIII]-emitting ionized gas are correlated. But at the same time, the column density of Na D does not necessarily reflect the amount of dense post-shock gas which is apparently where most of the excess H_2 emission is produced. Our finding is reminiscent of that by Guillard et al. (2012). These authors investigated shocks driven into neutral and molecular gas by the impact of a radio jet and found that while shock signatures were clearly present in both media, there was no simple relationship between the kinematics of the two components.

5 DISCUSSION AND CONCLUSIONS

In normal star-forming galaxies, the emission from warm ($T_{exc} \sim 100 - 1000$ K) molecular hydrogen is a minor bi-product of star-formation processes. However, in ULIRGs the tight correlation between H_2 emission and star-formation indicators breaks down, and these objects show on average several times more H_2 emission than their star formation rates would suggest. In this paper we use archival *Spitzer* mid-IR spectra to measure molecular hydrogen rotational emission of 115 ULIRGs in the IRAS 1 Jy sample. We then

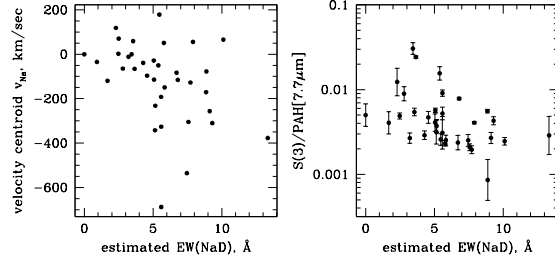


Figure 11. **Left:** Objects with strong Na D absorption are more likely to show high Na D blueshifts relative to the galaxy rest-frame ($p_S = 0.004$). **Right:** Excess H_2 may be associated with weaker Na D absorption (anti-correlation detected tentatively with $p_S = 0.08$).

use a number of morphological and spectral measurements at optical and infrared wavelengths to uncover the source of the excess H_2 emission. We use PAH luminosities as a star formation indicator and the H_2 /PAH ratios to quantify the amount of excess H_2 emission.

We find a surprising lack of evidence connecting H_2 emission with merger stages. There is no difference between the H_2 /PAH distributions of Pre-Mergers, Mergers, and Old Mergers; nor is there any correlation between H_2 /PAH and nuclear separation. This indicates that collision shock is not the primary source of the H_2 emission we observe. Perhaps the collision velocities of merging galaxies in ULIRG systems are insufficient to create the conditions necessary for the production of excess H_2 emission. Indeed, the most prominent example of H_2 excess associated with a collision shock involves a group-like environment and galaxy collision velocities $\sim 1000 \text{ km sec}^{-1}$ (Appleton et al. 2006), presumably much larger than the relative velocities of merging galaxies in our sample (Colina et al. 2001 estimate that the typical orbital velocity in ULIRGs in the advanced stage of merger is $\sim 250 \text{ km/sec}$).

With collision shocks ruled out as a primary mechanism for H_2 emission, we investigate other possible sources of H_2 excess in ULIRGs. We confirm that the primary mechanism of the rotational H_2 emission is shock excitation by finding a strong correlation between H_2 /PAH and optical shock diagnostics, such as $[O \text{ I}]\lambda 6300\text{\AA}/H\alpha$. We also find a positive correlation between H_2 /PAH and the widths of optical emission lines. Broadening of optical emission lines beyond the typical line widths associated with galactic rotation has been shown by many authors to be due to galactic outflows; thus, we conclude that excess H_2 seen in ULIRGs likely arises in outflows as well.

We find a weak correlation between H_2 /PAH and the length of tidal tails, especially in Merger-stage galaxies characterized by a single nucleus, but with strong merger signatures. This likely indicates that H_2 -producing outflows require some time to develop after the first close passage of the two merging galaxies. The median age of stellar populations in our sample is 250 Myr, consistent with the star-formation time scales in numerical simulations of major mergers. However, unfortunately we do not find any correlations between outflow diagnostics and the age of the stellar population, and thus we cannot pinpoint more precisely the most opportune time for the formation of the H_2 -producing outflows.

Furthermore, we find a strong correlation between H_2 and $[Fe \text{ II}]$, an emission feature strongly associated with shocks driven into a largely neutral medium. ULIRGs classified as star-forming galaxies and those containing powerful AGNs all lie on the same H_2 - $[Fe \text{ II}]$ sequence. Although the AGN-dominated objects tend to have

higher H_2 /PAH ratios, the effect of the AGN is fairly subtle (the distributions differ at 90 per cent confidence level, but not at 99 per cent confidence level), and we find it unlikely that direct emission from the AGN is responsible for the excitation of H_2 . Instead, we argue that in ULIRGs of all types excess H_2 emission is produced in strong shocks driven into the neutral interstellar medium either by supernova explosions, or by the radiative pressure of the powerful AGN, or by both. As was previously suggested using observations and numerical simulations (Narayanan et al. 2008; Rupke & Veilleux 2013), we find that the most striking difference between AGN-dominated and star-formation-dominated outflows is the outflow velocity, with maximum blueshifts $v_{02} \sim -1000 \text{ km sec}^{-1}$ for the former and $v_{02} \sim -500 \text{ km sec}^{-1}$ for the latter.

Using our observations, we arrive at the following picture for the origin of the H_2 excess in ULIRGs. When gas-rich galaxies merge, the gravitational potential of each of them is perturbed by the passing companion. The gas that was initially in the rotational equilibrium within each galaxy disk is now supplied to the centre; at the same time, the potential perturbations lead to the formation of tidal tails. This massive inflow of gas fuels an intense burst of star formation which starts at about the time of the first close approach and can continue at a heightened rate for hundreds of millions of years (Rich, Kewley & Dopita 2011; Torrey et al. 2012). The gas is continually supplied, new stars form (and the more massive of them explode as supernovae), and sometimes the conditions are fortuitous for strong AGN activity.

It appears that for the production of H_2 and $[Fe \text{ II}]$ emission, the exact powering source of outflow (supernova-driven vs AGN-driven) does not matter as much as the physical conditions into which the outflow propagates. Both supernovae and AGNs inject energy into the interstellar medium, leading to a formation of a bubble of hot gas that expands and drives the shocks into the rest of the interstellar medium (Cecil, Bland-Hawthorn & Veilleux 2002). Supernovae are active throughout the entire merger, as long as new stars continue to form, whereas the AGN phase tends to last only a short fraction of the merger sequence. However, the instantaneous energy injection by the AGN may be higher leading to higher outflow velocities in this phase (Narayanan et al. 2008).

As the outflow propagates into the interstellar medium of the galaxy, it impacts, shocks, entrains and shreds clouds of varying densities and sizes. Thus a wide range of physical conditions is represented within the outflow, including partially ionized regions where $[O \text{ I}]\lambda 6300\text{\AA}$ and $[Fe \text{ II}]$ emission is produced. The strongest correlations that we find are between the H_2 emission and these emission lines, indicating a strong likelihood that H_2 is excited in the same regions by supernova-driven and AGN-driven shocks.

ACKNOWLEDGMENTS

We thank J.E.Green, L.J.Kewley, N.P.H.Nesvadba, D.A.Neufeld and the anonymous referee for useful discussions, and D.-C.Kim, M.Imanishi and S.Veilleux for making their data electronically available. M.J.H. is supported in part by the Dean's Undergraduate Research Award (JHU) and the Provost's Undergraduate Research Award (JHU). N.L.Z. is supported in part by the Alfred P. Sloan fellowship and Theodore Dunham, Jr. Grant of the Fund for Astrophysical Research. This research has made use of the NASA/IPAC Infrared Science Archive and NASA/IPAC Extragalactic Database, which are operated by the Jet Propulsion Laboratory, California Institute of Technology, under contract with the National Aeronautics and Space Administration.

REFERENCES

- Allamandola L. J., Tielens A. G. G. M., Barker J. R., 1989, *ApJS*, 71, 733
- Appleton P. N. et al., 2006, *ApJL*, 639, L51
- Armus L. et al., 2006, *ApJ*, 640, 204
- Armus L. et al., 2007, *ApJ*, 656, 148
- Barnes J. E., Hernquist L., 1996, *ApJ*, 471, 115
- Barnes J. E., Hernquist L. E., 1991, *ApJL*, 370, L65
- Beirão P., Appleton P. N., Brandl B. R., Seibert M., Jarrett T., Houck J. R., 2009, *ApJ*, 693, 1650
- Binney J., Tremaine S., 2008, *Galactic Dynamics: Second Edition*. Princeton University Press
- Cecil G., Bland-Hawthorn J., Veilleux S., 2002, *ApJ*, 576, 745
- Chen Y.-M., Tremonti C. A., Heckman T. M., Kauffmann G., Weiner B. J., Brinchmann J., Wang J., 2010, *AJ*, 140, 445
- Cluver M. E. et al., 2013, *ApJ*, 765, 93
- Colina L. et al., 2001, *ApJ*, 563, 546
- Dale D. A., Helou G., 2002, *ApJ*, 576, 159
- Dasyra K. M., Combes F., 2011, *A&A*, 533, L10
- Dasyra K. M. et al., 2006, *ApJ*, 638, 745
- Davies R. I., Sternberg A., Lehnert M., Tacconi-Garman L. E., 2003, *ApJ*, 597, 907
- Diamond-Stanic A. M., Rieke G. H., 2010, *ApJ*, 724, 140
- Donahue M., de Messières G. E., O'Connell R. W., Voit G. M., Hoffer A., McNamara B. R., Nulsen P. E. J., 2011, *ApJ*, 732, 40
- Draine B. T., 2011, *Physics of the Interstellar and Intergalactic Medium*. Princeton, NJ: Princeton University Press
- Egami E. et al., 2006, *ApJ*, 647, 922
- Ellison S. L., Mendel J. T., Scudder J. M., Patton D. R., Palmer M. J. D., 2013, *MNRAS*, 430, 3128
- Farrah D. et al., 2007, *ApJ*, 667, 149
- Ferland G. J., Fabian A. C., Hatch N. A., Johnstone R. M., Porter R. L., van Hoof P. A. M., Williams R. J. R., 2008, *MNRAS*, 386, L72
- Guillard P., Boulanger F., Pineau Des Forêts G., Appleton P. N., 2009, *A&A*, 502, 515
- Guillard P. et al., 2012, *ApJ*, 747, 95
- Higdon S. J. U., Armus L., Higdon J. L., Soifer B. T., Spoon H. W. W., 2006, *ApJ*, 648, 323
- Hollenbach D. J., Tielens A. G. G. M., 1997, *ARA&A*, 35, 179
- Houck J. R. et al., 2004, *ApJS*, 154, 18
- Huber K. P., Herzberg G., 1979, *Molecular spectra and molecular structure. IV. Constants of diatomic molecules*. New York: Van Nostrand-Reinhold
- Imanishi M., Dudley C. C., 2000, *ApJ*, 545, 701
- Ingalls J. G., Bania T. M., Boulanger F., Draine B. T., Falgarone E., Hily-Blant P., 2011, *ApJ*, 743, 174
- Johnstone R. M., Hatch N. A., Ferland G. J., Fabian A. C., Crawford C. S., Wilman R. J., 2007, *MNRAS*, 382, 1246
- Kauffmann G., et al., 2003, *MNRAS*, 341, 33
- Kim D.-C., Sanders D. B., 1998, *ApJS*, 119, 41
- Kim D.-C., Veilleux S., Sanders D. B., 2002, *ApJS*, 143, 277
- Landau L. D., Lifshitz E. M., 1991, *Quantum mechanics: non-relativistic theory*. Oxford, Boston: Butterworth-Heinemann
- Liu G., Zakamska N. L., Greene J. E., Nesvadba N. P. H., Liu X., 2013a, *MNRAS*, 430, 2327
- Liu G., Zakamska N. L., Greene J. E., Nesvadba N. P. H., Liu X., 2013b, *MNRAS*, in press (arXiv:1305.6922)
- Mihos J. C., Hernquist L., 1994, *ApJL*, 431, L9
- Mihos J. C., Hernquist L., 1996, *ApJ*, 464, 641
- Moorwood A. F. M., Oliva E., 1988, *A&A*, 203, 278
- Morel T., Doyon R., St-Louis N., 2002, *MNRAS*, 329, 398
- Mouri H., Kawara K., Taniguchi Y., 2000, *ApJ*, 528, 186
- Mouri H., Taniguchi Y., Kawara K., Nishida M., 1989, *ApJL*, 346, L73
- Murray N., Chiang J., Grossman S. A., Voit G. M., 1995, *ApJ*, 451, 498
- Narayanan D. et al., 2008, *ApJS*, 176, 331
- Narayanan D. et al., 2010a, *MNRAS*, 407, 1701
- Narayanan D., Hayward C. C., Cox T. J., Hernquist L., Jonsson P., Younger J. D., Groves B., 2010b, *MNRAS*, 401, 1613
- Nesvadba N. P. H. et al., 2010, *A&A*, 521, A65
- Ogle P., Antonucci R., Appleton P. N., Whysong D., 2007, *ApJ*, 668, 699
- Ogle P., Boulanger F., Guillard P., Evans D. A., Antonucci R., Appleton P. N., Nesvadba N., Leipski C., 2010, *ApJ*, 724, 1193
- Peterson B. W. et al., 2012, *ApJ*, 751, 11
- Petric A. et al., 2010, in *Bulletin of the American Astronomical Society*, Vol. 42, American Astronomical Society Meeting Abstracts 215, p. 365.05
- Petric A. O. et al., 2011, *ApJ*, 730, 28
- Proga D., Stone J. M., Kallman T. R., 2000, *ApJ*, 543, 686
- Reach W. T. et al., 2006, *AJ*, 131, 1479
- Rich J. A., Kewley L. J., Dopita M. A., 2011, *ApJ*, 734, 87
- Rigopoulou D., Kunze D., Lutz D., Genzel R., Moorwood A. F. M., 2002, *A&A*, 389, 374
- Rosenberg M. J. F., van der Werf P. P., Israel F. P., 2012, *A&A*, 540, A116
- Roussel H. et al., 2007, *ApJ*, 669, 959
- Roussel H., Sauvage M., Vigroux L., Bosma A., 2001, *A&A*, 372, 427
- Rupke D. S., Veilleux S., Sanders D. B., 2002, *ApJ*, 570, 588
- Rupke D. S., Veilleux S., Sanders D. B., 2005, *ApJS*, 160, 115
- Rupke D. S. N., Veilleux S., 2013, *ApJ*, 768, 75
- Sanders D. B., Mirabel I. F., 1996, *ARA&A*, 34, 749
- Shull J. M., Beckwith S., 1982, *ARA&A*, 20, 163
- Smith J. D. T. et al., 2007, *ApJ*, 656, 770
- Solomon P. M., Downes D., Radford S. J. E., Barrett J. W., 1997, *ApJ*, 478, 144
- Soto K. T., Martin C. L., Prescott M. K. M., Armus L., 2012, *ApJ*, 757, 86
- Spoon H. W. W., Marshall J. A., Houck J. R., Elitzur M., Hao L., Armus L., Brandl B. R., Charmandaris V., 2007, *ApJL*, 654, L49
- Strauss M. A. et al., 2002, *AJ*, 124, 1810
- Toomre A., Toomre J., 1972, *ApJ*, 178, 623
- Torrey P., Cox T. J., Kewley L., Hernquist L., 2012, *ApJ*, 746, 108
- Turner J., Kirby-Docken K., Dalgarno A., 1977, *ApJS*, 35, 281

- Veilleux S., Kim D.-C., Sanders D. B., 1999, ApJ, 522, 113
Veilleux S., Kim D.-C., Sanders D. B., 2002, ApJS, 143, 315
Veilleux S., Rupke D. S. N., Swaters R., 2009, ApJL, 700, L149
Veilleux S., Sanders D. B., Kim D.-C., 1997, ApJ, 484, 92
Whittle M., 1985, MNRAS, 213, 33
York D. G., et al., 2000, AJ, 120, 1579
Yuan T.-T., Kewley L. J., Sanders D. B., 2010, ApJ, 709, 884
Zakamska N. L., 2010, Nature, 465, 60